Progress in Additive Manufacturing (2025) 10:3361–3375
https://doi.org/10.1007/s40964-024-00818-3

FULL RESEARCH ARTICLE

Advancing powder bed fusion-laser beam technology: in-situ layerwise thermal monitoring solutions for thin-wall fabrication

Vito Errico[1] · **Fania Palano**[2] · **Sabina Luisa Campanelli**[1]

Received: 29 February 2024 / Accepted: 18 September 2024 / Published online: 26 September 2024
© The Author(s) 2024

Abstract
Additive manufacturing (AM) technologies, particularly powder bed fusion-laser beam (PBF-LB/M), offer unique capabilities in producing intricate components directly, leading to streamlined processes, cost reductions, and time savings. However, inherent challenges in AM processes necessitate advanced monitoring systems for fault detection and quality assurance. This study focuses on the development and application of in-situ, layer-by-layer thermal monitoring solutions to detect defects such as localized overheating and inadequate fusion in thin-walled components produced by PBF-LB/M. An optimal setup using an off-axis IR thermal camera was devised to monitor the entire slice during processing. Thermographic data, analyzed using MATLAB, identified thermal parameters indicative of process efficiency and print quality. Micro-tomographic scans on finished products correlated defects with thermographic data. Results showed influences of sample thickness on maximum temperatures, effects of powder bed thickness on process temperatures, and identified geometric distortions in inclined walls due to high thermal stress. Three-dimensional thermograms enabled comprehensive temperature distribution analysis, crucial for quality control and defect detection during construction. Insights from this study advance thermographic analysis for PBF-LB/M processes, providing a foundational framework for future additive manufacturing monitoring and quality control enhancements.

Keywords Powder bed fusion-laser beam · Thermal monitoring · Thin walls · Micro-tomography

1 Introduction

Additive manufacturing (AM) has long been regarded as a prominent method for component production, offering the unique capability to fabricate intricate three-dimensional parts directly. This ability not only streamlines manufacturing processes but also yields cost reductions and time savings [1–3]. However, in recent years, AM has faced challenges attributed to inherent process issues [4]. Conversely, within the current manufacturing landscape, smart manufacturing has emerged as a transformative paradigm. It encompasses the integration of advanced methodologies and technologies, aiming to optimize production processes. Notably, AM has increasingly adopted intelligent methodologies, leveraging in-situ sensors, diagnostics, and online/offline monitoring systems. These systems are designed to detect faults or anomalies during the manufacturing process. By harnessing artificial intelligence for autonomous decision-making, this approach effectively mitigates material waste, reduces energy consumption, and minimizes process downtime, thus ensuring uninterrupted regulation of the manufacturing process [5, 6]. The convergence of AM with intelligent methodologies has propelled notable advancements in AM processes. This is particularly evident in the realm of powder bed fusion-laser beam (PBF-LB/M) technology [5, 7, 8]. As per the ASTM 52900:2015 standard, PBF-LB/M is a technique that uses a high-energy laser to fuse metallic particles layer by layer [9]. Given the myriad of variables that impact the PBF-LB/M process, real-time and in-situ monitoring tools have become essential to maintain stringent quality standards and maximize productivity while minimizing waste [10]. These tools are designed to detect specific process signatures and associate them with specific defects or inaccuracies within the manufacturing process. They also serve as the foundation for more advanced real-time

✉ Vito Errico
vito.errico@poliba.it

[1] Department of Mechanics, Mathematics and Management, Politecnico di Bari, Via Orabona 4, 70125 Bari, Italy

[2] ENEA, Centro Ricerche di Brindisi c/o Cittadella della Ricerca, S.S.7 Appia km 706, 72100 Brindisi, Italy

monitoring systems capable of automatically detecting and classifying anomalies as they occur [11, 12]. Such capabilities are essential for real-time control and adjustment of manufacturing processes to ensure optimal results [13]. Therefore, the integration of input parameters, process sensor data, and comprehensive part analysis along with an adaptive decision framework facilitates rapid optimization of both the final product and manufacturing parameters [5]. Consequently, efforts to refine the control of the AM manufacturing process include a significant focus on the innovation of novel process sensors, the improvement of current detection methods, and the evaluation of the most effective combination of sensors tailored to specific processes, materials, or components [5]. Within the realm of the PBF-LB/M process, certain geometries present distinct challenges due to their critical nature. These challenges include components with overhanging structures, thin geometries and sharp angles [14]. These geometries entail specific process conditions, wherein the melt pool generated by the laser beam, during the scanning of such geometries, finds itself surrounded by virgin powder with lower conductivity compared to the solid material [15]. Consequently, local overheating phenomena occur in overhanging regions and in angles, which generate defects such as raised edges and/or local geometric distortions. To address these issues, the PBF-LB/M process typically involves the insertion of support structures aimed at allowing heat dissipation in these critical regions [16, 17]. However, such geometries would lead to prolonged manufacturing times and distortions during their detachment from the final component [16]. A notable challenge arises when constructing structures with protruding surfaces without the use of supports. In these cases, the overhanging areas are built on unfused metal powder, impacting the physical mechanisms occurring during the PBF-LB/M process [14]. This results in prolonged solidification times for the molten pool, slower heat transfer, and a higher concentration of heat in the laser beam irradiation zone [18]. Consequently, local sintering of the powder occurs, resulting in surface roughness and geometric distortions that compromise the quality of the final component [19, 20]. While several studies have focused on identifying optimal process parameters and scanning strategies to mitigate these defects and improve the fabrication of overhanging surfaces, there remains a lack of literature examining the in-process monitoring of these structures [18]. In addition, detecting geometric distortions caused by variations in wall thickness and building angle remains an area for exploration. Krauss et al. [21, 22] conducted a comprehensive investigation utilizing thermal imaging technology to analyze alterations in thermal patterns resulting from changes in processing parameters. Their study specifically examined the effects of scanning vector length, laser power, and layer thickness on the thermal distribution within specimens. Through meticulous analysis of key indicators across layers, they developed a robust three-dimensional quality assessment method for detecting defects during the solidification process. Similarly, Bartlett et al. [23] addressed critical inquiries regarding infrared (IR) monitoring in PBF-LB/M processing. Their research successfully employed IR monitoring to identify lack of fusion defects in PBF-LB/M parts. Notably, they emphasized the significance of defect size in IR imaging detectability and proposed enhancements in spatial resolution and camera positioning. Furthermore, their findings showcased the potential of full-field IR monitoring to improve PBF-LB/M part qualification methods, facilitating real-time defect detection and process consistency analysis. Our study builds upon these works by addressing the gaps identified in the existing literature. Specifically, we focus on implementing and applying in-situ, layer-by-layer thermal monitoring methodologies (monitoring systems combined with image processing) to detect defects such as geometric distortions, localized overheating and inadequate fusion. By meticulously monitoring the 2D temperature profile across each layer, our research aims to improve the precision, efficiency, and overall quality of AM processes. In doing so, we contribute to the advancement of additive manufacturing technology and pioneer more precise control, increased efficiency, and higher quality standards in the industry. By addressing critical gaps in the literature and pushing the boundaries of in-process monitoring technology, our study aims to realize innovative advances in additive manufacturing technology. This research effort circles back to the critical study of the "slice" process signature and the meticulous identification of the aforementioned defects. As highlighted by Colosimo et al. [8], navigating these interrelationships is a significant challenge within the scientific literature. Few studies, mentioned earlier, have been conducted on this topic. This is primarily due to the existing limitations in commercialized thermal monitoring systems (utilization of low spatial resolutions to achieve extensive field of view (FOV) sizes for monitoring the entire slice and low data acquisition frequencies to strike a balance between the necessary information and manageable file sizes) and the complexities involved in extracting accurate quantitative data related to the thermal evolution of components produced by the PBF-LB/M process. Practical limitations related to the experimental setup, including space constraints and data acquisition times, also needed to be considered. Ultimately, our efforts aim to advance the field and enable more precise control, increased efficiency, and higher quality standards in additive manufacturing.

The study followed a structured approach. First, the main parameters of the PBF-LB/M process and the geometry of the parts were defined. In particular, the focus was on the production of "thin walls" with variations in thickness and inclination relative to the building axis. The aim was to evaluate the process stability during the production of thin-walled

components, especially as the inclination increase and thickness decrease. An optimal setup was then devised to implement the monitoring system, using an IR thermal camera in an off-axis configuration to monitor the entire slice during processing. An image acquisition rate of 100 Hz has been set, with an integration time of 50 µs. This choice allowed to observe a temperature range between 260 and 1100 °C. Thermographic data were captured and immediately analyzed using MATLAB to detect different wall behaviors and identify thermal parameters indicative of process efficiency and print quality. In addition, micro-tomographic scans were performed on finished products to identify defects and potential correlations with thermographic data.

2 Materials and methods

2.1 Experimental setup and materials for PBF-LB/M process

Experiments were conducted using the concept laser M1 plant, which was equipped with a solid-state laser (Nd: YAG, diode-pumped) with the following parameters: a wavelength of 1064 nm, a maximum laser power of 100 W, and a laser spot diameter of 200 µm. The machine was operated using two interfaced software programs, one for the machine and one for the laser. The laser beam, guided by a PC-controlled scanning system and galvanometric mirrors, fuses the powder particles on a powder bed surface using slicing data from Magics® 11 software. Nitrogen was also introduced into the chamber to reduce oxidation and maintain the initial oxygen level below 0.8%. The stainless steel powder used in this study is AISI 316L, supplied by Mimete metal powders (Italy). The powder exhibited a spherical morphology and had particle sizes ranging from 15 to 45 µm. It was produced through gas atomization.

2.2 Experimental plan: PBF-LB/M of straight and inclined thin walls

In this study, thin walls were fabricated by varying two geometric parameters: wall thickness and inclination relative to the build direction (z-axis). The other two dimensions of the wall were set at 10 mm for height and 30 mm for length. Two different printing batches were produced: straight walls (with a building angle of 0°) and inclined walls (with a building angle of 45°); the latter was chosen because it represents a critical inclination for the PBF-LB/M process, generating defects [24] and thus being interesting to monitor. Table 1 displays the complete experimental plan. Both batches were manufactured using process parameters optimized in previous works, as mentioned in Table 2 [25, 26]. The scanning strategy was selected to maximize the local overheating phenomena occurring in overhanging regions and angles, which lead to defects such as raised edges and/or local geometric distortions. Specifically, a unique scanning strategy was adopted for all fabricated walls, involving "contour" scanning followed by "core" scanning. For "core" scanning, a random island scanning strategy, patented by Concept Laser, was chosen. This scanning strategy reduces thermal stresses by dividing the core into smaller islands, creating a grid. These islands, whose optimal size to mitigate residual stresses mentioned in the literature is 5×5 mm^2 [27–29], are scanned in random order with parallel vector tracks oriented at 45° to the principal directions of each island. Finally, in the subsequent layer, the islands are shifted by 1 mm in both the x and y directions to prevent the formation of fusion voids at the edges of the islands as the layers progress. Figure 1 illustrates the thin walls produced in this study.

2.3 Systems and procedures for thermal monitoring and computed tomography

Thermal monitoring during the PBF-LB/M process is crucial for identifying defects and optimizing parameters. In this study, a FLIR SC7200 cooled thermal imaging camera with a mid-infrared sensor was employed outside the machine (see Fig. 1c). The camera, with a high acquisition speed and < 25 mk at 25 °C NETD, captured thermal and radiometric measurements. The camera has a programmable image acquisition rate up to 190 Hz and a resolution of 320×256 pixels. The camera used Altair proprietary software for remote control and real-time observation. To optimize thermal monitoring, the camera was placed off-axis externally

Table 2 Processing parameters for PBF-LB/M experimental tests

Processing parameter	Notation	Unit	Value	
			Contour	Core
Laser power	P	W	100	100
Laser scan speed	V_s	Mm s^{-1}	180	200
Layer thickness	L_t	µm	30	30
Hatch distance	H_d	µm	–	140

Table 1 Design of experiment: geometric parameters and relative levels varied for the thin-wall fabrication

Geometric parameters	Notation	Unit	Factor levels				
			WT1	WT2	WT3	BA1	BA2
Building angle	BA	°	–	–	–	0	45
Wall thickness	WT	mm	1	3	5	–	–

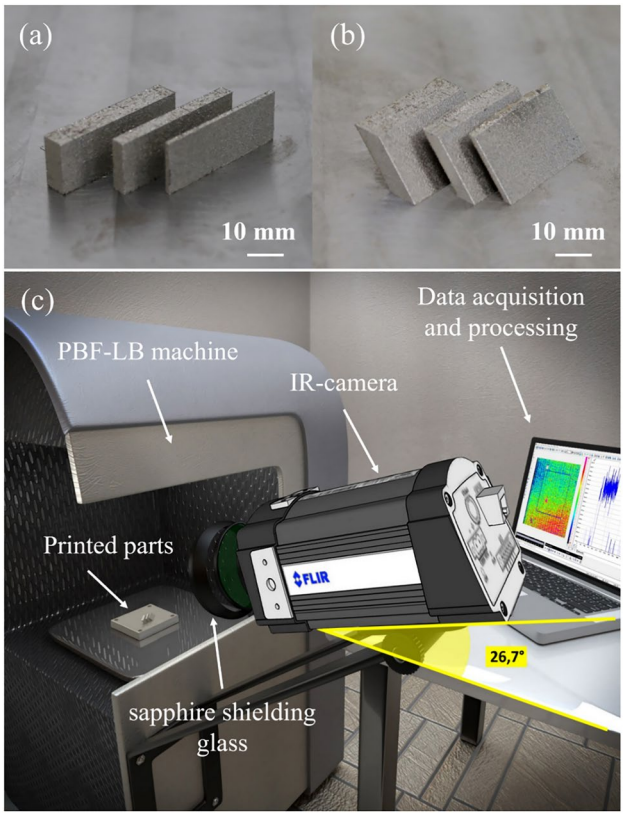


Fig. 1 **a, b** Visual representations of the thin walls produced through the PBF-LB/M manufacturing technique. **c** Overall configuration of the thermal monitoring setup: mid-wavelength infrared (MWIR) thermal imaging camera, sapphire shielding glass and data acquisition and processing desktop

due to limited access inside the build chamber. It was angled at 26.7° to the building platform and equipped with a 25 mm focal length lens with an f/2 aperture. This configuration provided a horizontal field of view (HFOV) of 22° and a vertical field of view (VFOV) of 17°. With known viewing angles and lens distance, an instantaneous field of view (IFOV) of approximately 0.5 mm/pixel was determined. In addition, filtering lenses were employed to evaluate different wavelengths, ensuring precise temperature measurements and accurate thermal imaging during the PBF-LB/M process. The employed thermal camera can detect temperatures up to 2500 °C, but the actual range depends on the integration time (IT), according to the calibration curves provided by the manufacturer. An integration time of 50 µs was set. This selection allowed to detect temperatures in the range 260–1100 °C. To accurately calibrate the camera, extensive literature review was conducted, reflecting on studies such as Refs. [30, 31], which highlighted the challenges of real-time temperature measurement and emphasized the importance of emissivity considerations. Emissivity, a critical parameter in thermal imaging, denotes an object's ability to emit thermal energy and varies based on surface properties, material composition, and temperature. In practice, determining the exact emissivity is complex due to material heterogeneity and temperature variability. For this study, an approximate emissivity value ($\varepsilon = 0.35$) was assumed based on prior research [25, 32] on AISI 316L powder material. This value, though constant across temperatures, was deemed appropriate for capturing temperature variations within the powder bed, considering the limitations posed by pixel size and melt pool dimensions. Furthermore, to ensure efficient data acquisition without compromising resolution, the camera's acquisition interval was meticulously optimized. Given the rapid nature of the PBF-LB/M process, a frame rate of 100 Hz was selected for real-time monitoring, striking a balance between the amount of necessary information and manageable file sizes. This choice was guided by the need to observe the powder bed around the building area, according to considerations outlined in Refs. [30, 31]. The thermal imaging setup, although positioned externally due to space constraints within the build chamber, was meticulously calibrated to ensure accurate temperature measurements. The original glass, transparent to visible light but not to the laser wavelength, was replaced with a new one transparent to radiation in the 1–5 µm range. A 7-mm-thick sapphire glass was installed, which is particularly suitable for this application. Sapphire is transparent to infrared radiation across a broad range of wavelengths, ensuring that it does not affect the measurements. The camera's advanced features, coupled with rigorous calibration protocols and optimization strategies, enabled comprehensive thermal monitoring throughout the PBF-LB/M process, facilitating detailed analysis of temperature distributions and defect identification.

For computed tomography, a GE Phoenix 'nanotom s' system was utilized. This system employed a high-performance nano-focus X-ray tube (180 kV/15 W) with a tungsten or molybdenum transmission target. Equipped with a 5-megapixel CMOS detector, it produced 2D X-ray images with a pixel size of 50×50 µm^2 and a dynamic range of 12 bits. The selected magnification of 2.5 times resulted in a resolution of 20 µm. During each scan, 1800 radiographs were recorded with an angular step of 0.20°, and each X-ray was averaged from three acquisitions to improve signal-to-noise ratio. The total acquisition time for each scan was approximately 2 h. These systems and methodologies provided comprehensive thermal monitoring and computed tomography for in-depth analysis of the PBF-LB/M process and characterization of manufactured samples.

2.4 Data analysis methodology

This section provides a detailed discussion of the data analysis techniques and methodologies devised to characterize the identified case study, along with addressing critical printing issues detected using an off-axis thermal monitoring system.

Multiple algorithms were developed using MATLAB to process the thermographic data gathered during the PBF-LB/M process. These MATLAB routines, custom-built for the study, are standardized to facilitate their application in other PBF-LB/M thermographic analyses, aiming to establish a consistent approach for processing in-situ and real-time thermographic data. Specifically, the following analyses were conducted:

- Evaluation of the temperature profile across the entire slice area.
- Determination of the maximum temperature attained.
- Assessment of geometric distortions.

All routines offer the following capabilities:

- Generating results as a function of time (or frames acquired) based on the input acquisition frequency.
- Adapting the graphs to reflect the actual deposition process instead of considering the entire acquisition period.
- Adjusting the graphs according to the temperature calibration range.
- Modifying the graphs to suit the geometries under analysis.

2.4.1 Temperature variation over time

An analysis of temperature trends and distributions during the printing process serves as the initial steps in the examination of thermographic data. Understanding temperature readings is crucial for comprehending the melting and solidification phenomena inherent in the process. The first implemented routine evaluates the maximum temperature trend of the image over time, providing qualitative insights into the thermal behavior of the observed area. By analyzing this trend, distinct phases of the process, namely contour scanning (A) and core scanning (C), can be identified. These phases involve scanning the contour (A) of the walls followed by a pause (B) before scanning the core (C), as per the predetermined strategy (see Fig. 2).

However, due to overlapping temperature fields between different samples and phases, it is challenging to evaluate the thermal cycle of each wall separately. Algorithms were developed to calculate the durations of individual phases and identify corresponding layers in the processed images, taking advantage of the laser beam's moments inactive. In addition, an algorithm was devised to identify the layers corresponding to the processed images by extrapolating information from the laser machine's log file. This facilitated matching camera videos with specific layers of the printing process. These methodologies enhance the understanding of temperature dynamics during printing, laying the groundwork for further analysis.

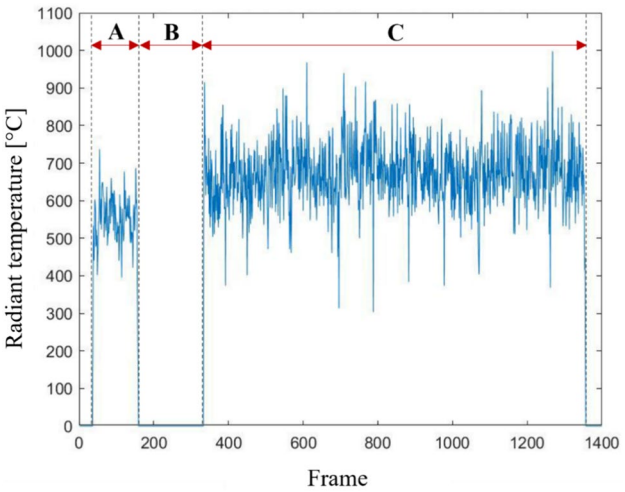


Fig. 2 An illustration of the highest temperature profile for the 125 layer of straight thin walls over the whole slice area

2.4.2 Image processing

A routine was developed to analyze the thermogram corresponding to a generic frame, enabling observation of the movement of the laser beam and resulting surface thermal signature as frames change. This visualization was essential for understanding what could be monitored based on the thermal camera's resolution. However, due to the camera's limited resolution, precise monitoring of parameters related to the melt pool was not feasible, as the melt pool size was smaller than a single pixel (200 µm and 500 µm, respectively). It should be noted that the "real" temperature cannot be determined in the absence of precise information on the emissivity value. Therefore, the following graphs represent radiant temperature rather than true temperature. The camera's calibrated "radiant" temperature range and color scale range were 260–1100 °C. Figure 3 illustrates the sequence of image processing steps implemented in this study. To provide a comprehensive view of the process, an algorithm was implemented to generate a "global" thermogram, representing the maximum temperature reached in each pixel of the slice (see Fig. 3a). Increasing image resolution was employed to improve thermogram clarity, with interpolation techniques used to distribute temperatures among newly created pixels (see Fig. 3b). However, this image often contained background noise due to spatters, a typical defect in PBF-LB/M processes. Masks were applied to eliminate spatter-related noise, enhancing image clarity (see Fig. 3c). This ensured accurate removal of spatters throughout the printing process. In Fig. 3d, the resulting thermographic map with isotherms added provides a detailed visual representation of the geometry and temperature distribution of the realized slice. In addition, to address the movement of inclined walls during printing, an automated algorithm was

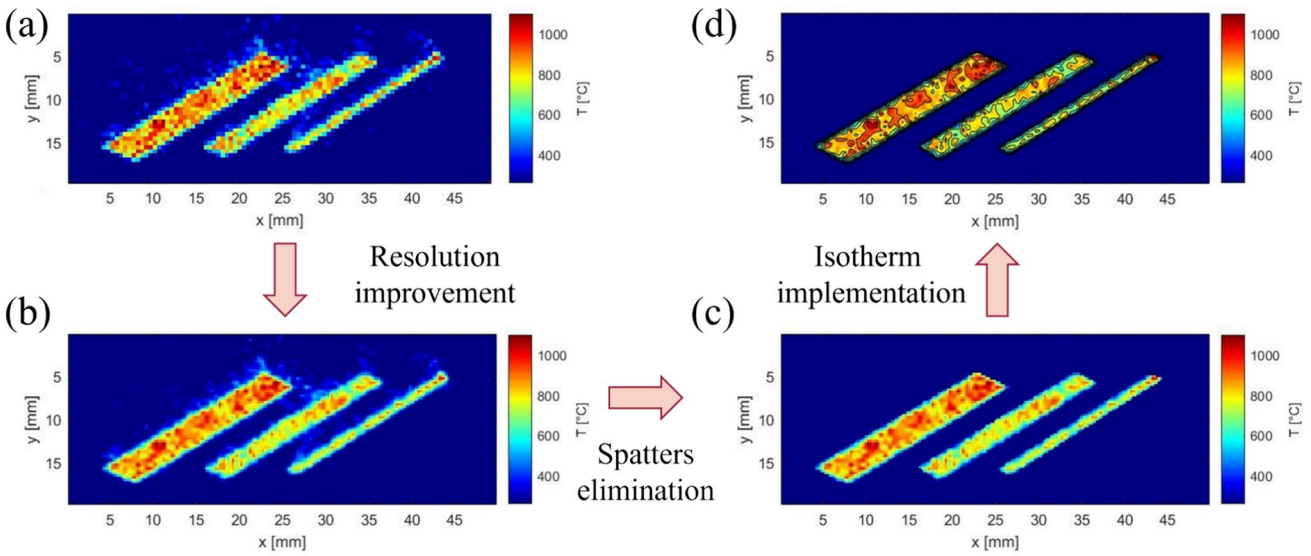


Fig. 3 **a** Global thermographic map with a resolution equal to 100×40 pixels. **b** Global thermographic map with a resolution equal to 200×80 pixels. **c** Removal of spatters through mask application. **d** Isotherms applied to a generic thermographic map of a slice representing straight walls

devised to identify characteristic points in each layer and adjust masks accordingly (see Fig. 4). The resulting thermographic maps provided a comprehensive depiction of slice geometry and temperature distribution. It is important to note that the graphs presented are based on the original image resolution to save temperature accuracy derived from the thermal camera.

3 Results and discussion

3.1 Thermal examination of straight thin walls

After processing the thermogram images depicting the maximum temperature reached in each pixel, the individual straight walls with thicknesses of 5 mm, 3 mm, and 1 mm underwent detailed thermal analysis. To ensure a comprehensive examination, the contouring and core scanning phases were studied separately. This involved utilizing the algorithm described in Sect. 2.4.1 to process the thermograms for each phase independently. The algorithm facilitates the sequential analysis of the contour and core scanning phases, providing valuable insights into the thermal behavior of the walls.

3.1.1 Thermal investigation of straight thin walls during the contour scanning phase

With knowledge of the initial and final moments of the slice perimeter scan, the corresponding maximum temperature distribution in the XY plane was defined, as shown in Fig. 5a. It is notable that for the 1-mm-thick wall, detecting the core area with this representation was particularly challenging. In addition, the infrared camera was unable

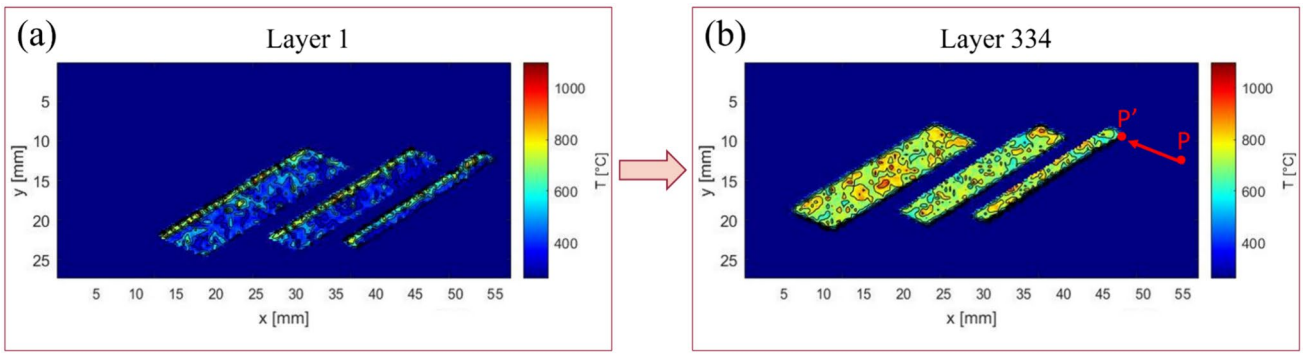


Fig. 4 Inclined thin walls: **a** global thermographic map of the layer 1; **b** global thermographic map of the final layer

to detect temperatures higher than the melting temperature (~ 1450 °C) at any point in the scan. This limitation is attributed to the low resolution of the sensor, indicated by the high pixel size in relation to the size of the melt pool. Furthermore, the calibration curve of the chamber correctly detects temperatures in the 260–1100 °C range. The variation in temperature distribution across different layers and walls of varying thicknesses was of interest. To assess this, the average maximum temperature as the layers varied was evaluated. This parameter calculates the average value of the maximum temperatures reached at all points of the analyzed wall for a given layer. It is important to note that only pixels with a non-zero temperature were considered in this calculation. Comparing the results for the three straight walls summarized in Fig. 5b, a noticeable temperature increase is observed for the 1-mm-thick wall compared to thicker walls. This behavior can be explained by the extreme proximity between the two larger sides of the perimeter, resulting in a greater accumulation of heat. This observation aligns with findings reported in literature [33], which suggest that an increase in hatch distance leads to a reduction in the sensor's signal (temperature). On the other hand, analyzing the contour of the 3 mm and 5 mm walls did not reveal significant differences, as the thickness was sufficient to prevent substantial heat build-up. Figure 5a shows that the two larger sides of the contour are well spaced in both cases.

3.1.2 Thermal investigation of straight thin walls during the core scanning phase

With knowledge of the initial and final instants of the core scanning phase, it became possible to evaluate the

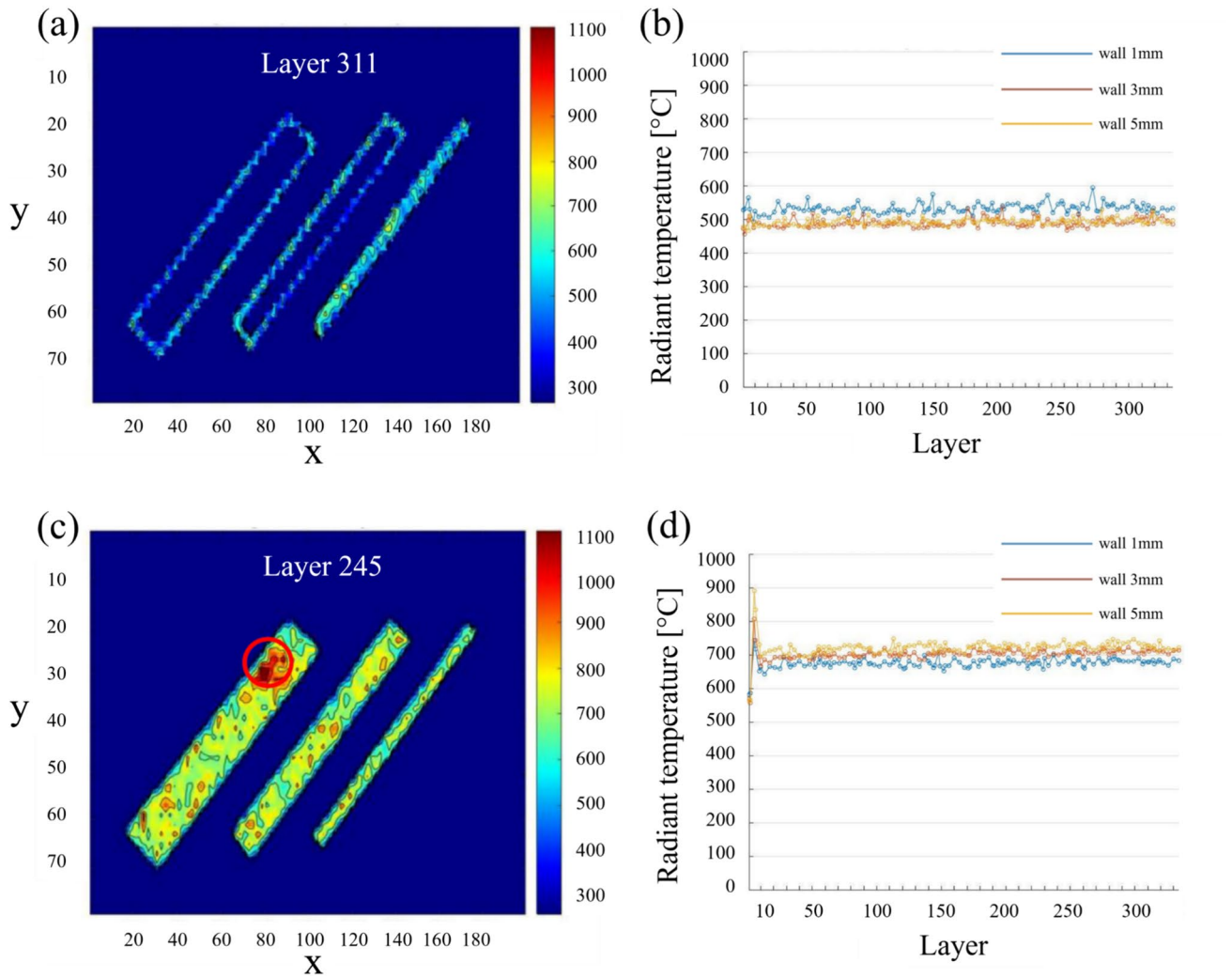


Fig. 5 **a** Global thermogram representing the contour phase of the straight thin walls layer 311. **b** The contour phase's average maximum temperature for the straight thin walls. **c** Global thermogram representing the core phase of straight thin walls layer 245. A red area indicates where heat is accumulating. **d** The core phase's average maximum temperature for the straight thin walls

temperature distribution among the various samples and at varying build heights. An example of temperature distribution at a generic build height is depicted in Fig. 5c; circled in red is highlighted the area with higher temperatures than the rest of the surface. This behavior could stem from the presence of defects like lack of fusion and porosity in the underlying layers, hindering heat dissipation towards lower layers. Studies, such as the one referenced in Ref. [21], associate this phenomenon with unidirectional heat dissipation towards the lower layers due to the presence of unmelted powder and voids, which have lower thermal conductivity compared to the solidified material. Similar to the contour analysis, the average maximum temperature for all three specimens during the core scanning phase was examined (Fig. 5d). This analysis revealed an initial peak followed by signal stabilization. The first slice, made without powder, recorded low temperatures due to the high thermal conductivity of the substrate. The subsequent temperature increase observed for the first 10 layers (as seen in Fig. 6a) is linked to a 150% increase in powder bed thickness. This adjustment, known as the 'dose step', aims to improve powder bed distribution at the start of the process until a stable regime is reached for the recoating phase. As highlighted in the study by Pavlov et al. [33], the temperature increase with powder bed thickness is attributed to the energy balance between powder melting and heat loss in the substrate or previously fabricated layer. The lower thermal conductivity of the powder bed, due to gaps between particles hindering heat transfer, leads to heat build-up difficult to dissipate to lower layers. This phenomenon is most visible in the first 10 layers, reflecting the temperature distribution in Fig. 6a, and becomes less pronounced in subsequent layers, as shown in Fig. 6b. In addition, as the wall thickness increases, there is a corresponding rise in temperature perceived by the thermal imaging camera. This trend is linked to the presence of larger islands as the wall thickness increases, resulting in greater heat accumulation. In Fig. 6c, scanning islands are depicted by red squares with 45° inclined vectors, while sample sections are represented by thicker black rectangles. The portion of the island affecting the core increases with wall thickness, contributing to the temperature increase, especially notable in the first 10 layers, as depicted in Fig. 6a, becoming less pronounced in subsequent layers.

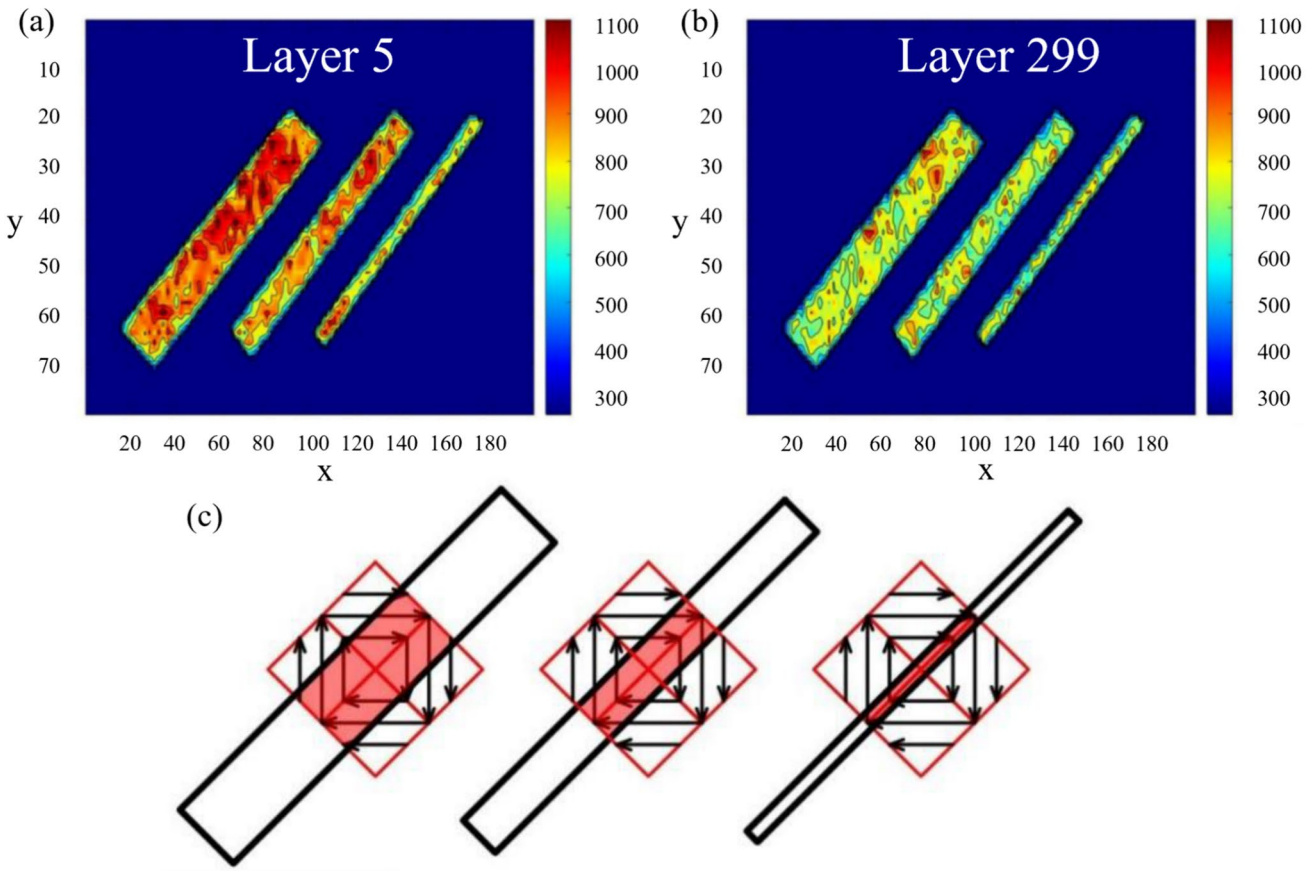


Fig. 6 Global thermographic maps: **a** layer 5 with a 150% dose step increase; **b** layer 299 without layer thickness increase. **c** The real section of the island that was scanned for the three thin walls investigated

3.1.3 3D thermograms analysis of straight thin walls

Three-dimensional thermograms were generated by overlaying two-dimensional heat maps to gain a comprehensive understanding of the temperature profile across the entire slice area at varying construction heights. This approach allows for a clearer visualization of the vertical development of the manufactured samples and facilitates the identification of overheated zones in 3D space. In Fig. 7, with reference to the color bar, it is evident that the contour of the individual thin walls exhibits lower temperatures compared to the inner core area. The theoretical volume of the individual walls is outlined by black segments, and no geometric distortions were observed for the samples depicted. However, due to the high pixel size of the thermal imaging camera, no direct correlation between superheated areas and porosity could be established. Analysis of porosity was conducted using microtomographic analysis instrumentation, as discussed in Sect. 2.3.

3.2 Thermal examination of inclined thin walls

Similarly to the analysis conducted for the straight thin walls, surface temperature distributions were acquired for the inclined thin walls, and both the contour and core scanning phases were thoroughly examined. In addition, due to the non-perpendicular growth of the building plane, the two major sides characterizing the three fabricated specimens were analysed separately. This approach allowed for a detailed investigation into the thermal behavior of the inclined thin walls during both the contour and core scanning phases.

3.2.1 Thermal investigation of inclined thin walls during the contour scanning phase

By identifying the initial and final instants of the slice perimeter scan, it was possible to establish the maximum temperature distribution in the XY plane, as illustrated in Fig. 8a. Unlike straight thin walls, in inclined thin walls, one of the two largest sides consistently exhibits higher temperatures than the other. This observation was consistent across all three samples of varying thicknesses. The vertical inclination of the walls leads to the presence of a protruding side (overhang), continuously built up on powdery material rather than on previously solidified layers. The lower thermal conductivity of the powdery material compared to the solid state contributes to heat accumulation on the overhang side [14], depicted as red, compared to the non-overhang side, shown in blue (see Fig. 8a). Examining the average maximum temperature variation during the contouring phase (Fig. 8b), a nearly constant trend is observed. The effect of the overhang side is balanced by the lower temperatures of the non-overhang side. Unlike straight walls, no significant differences are observed between different sample thicknesses, as the two larger sides of the perimeter are sufficiently spaced to avoid heat build-up or measurement errors. This outcome is attributed to the increased cross-sectional width of the inclined samples compared to straight ones. Given the oblique growth of the samples, analyzing the two largest sides forming the perimeter of the wall slice separately was of interest. In Fig. 9a–c, it is evident that for all three thin-wall thicknesses, the overhang section consistently exhibits higher temperatures than the non-overhang section. This behavior is due to the inclined development of the wall, where the overhang side is built on powder rather than on previously solidified material, leading to slower heat conduction and higher absorbed energy [34]. For the 5-mm and 3-mm-thick specimens, there is a steady average temperature

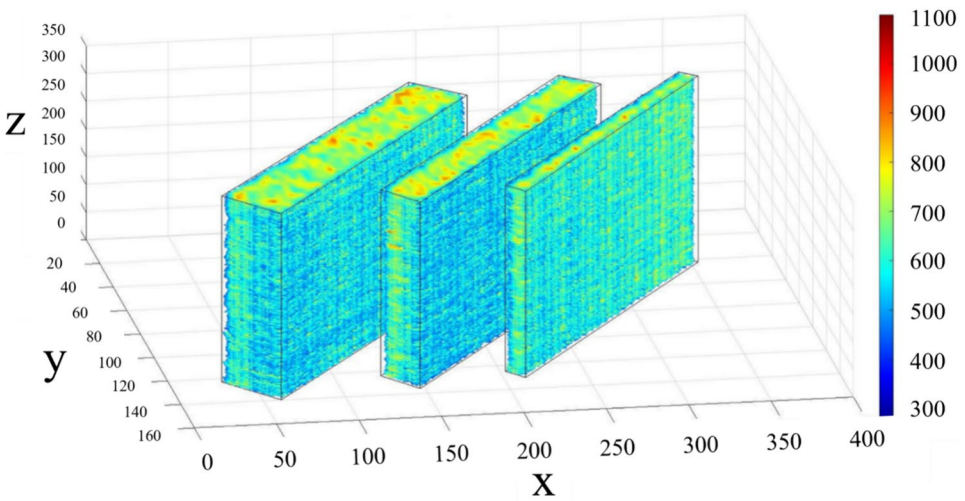


Fig. 7 Straight thin walls: 3D thermograms

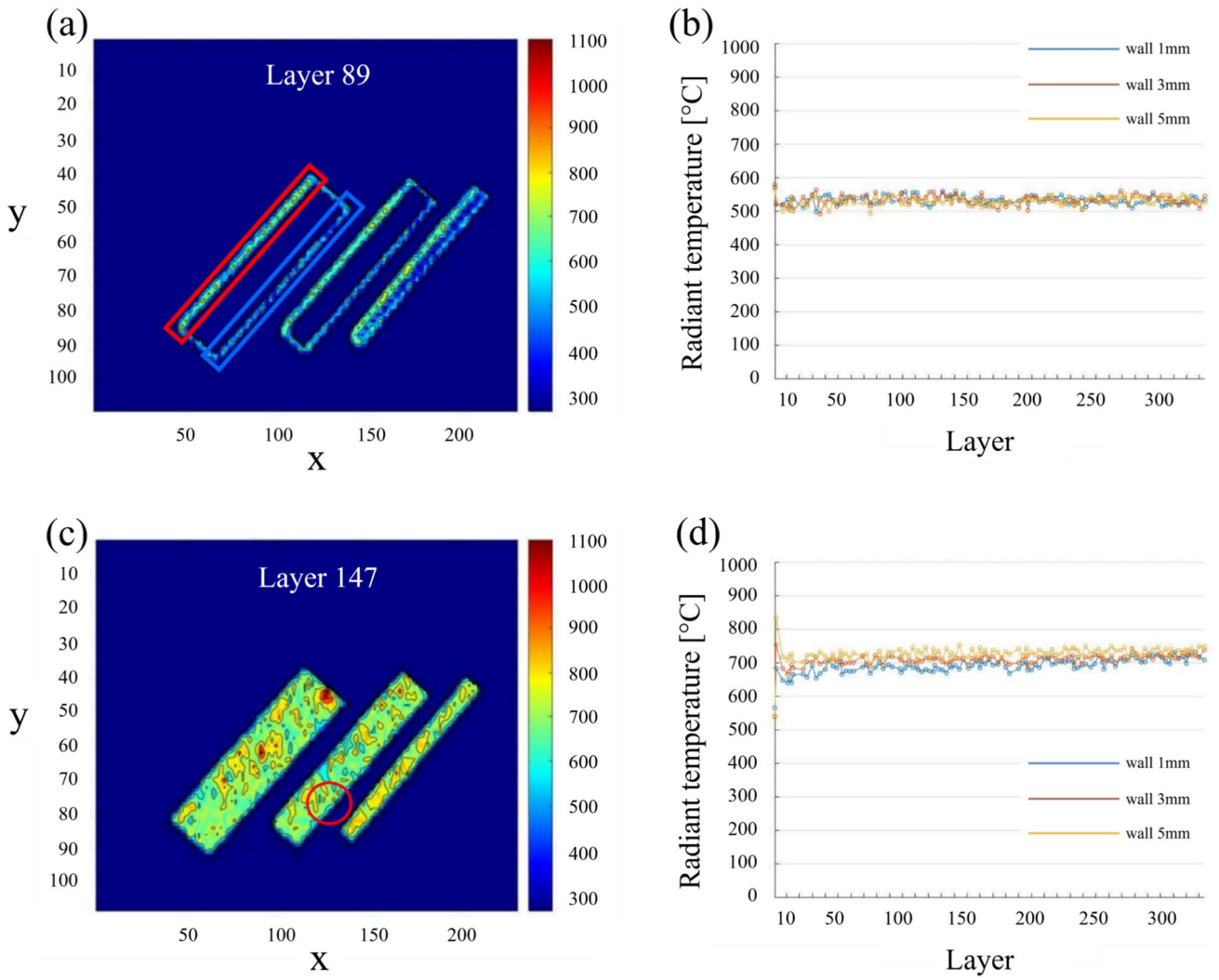


Fig. 8 **a** Global thermogram representing the contour phase of the inclined thin walls layer 89. **b** The contour phase's average maximum temperature for the inclined thin walls. **c** Global thermogram representing the core phase of inclined thin walls layer 147. A red area indicates where heat is accumulating. **d** The core phase's average maximum temperature for the inclined thin walls

trend for both sides of the contour. However, the 1 mm specimen shows an unusual trend, with decreasing temperatures on the overhang section (hot side) and increasing temperatures on the non-overhang section (cold side). This anomaly is attributed to increasing geometric distortions with construction height. The vertical distortion on the overhang side reduces the powder bed thickness locally, leading to reduced temperatures due to hindered remelting. In addition, a distortion in the XY plane causes the hot side to deviate from the inspection zone (mask), resulting in reduced temperatures (see Fig. 10a, b). On the 1 mm non-overhanging side (cold side), a bending in the XY plane causes part of this side to be built on powder rather than on the previous layer, explaining the temperature increase. Figure 10c, d provides a schematic representation of the distortion phenomenon in the XY plane, illustrating how temperature increases occur when the laser scanning path of layer n + 1 does not overlap with the previously constructed layer n but with the powder. Thermal stress build-up during manufacture can lead to stress and distortion in components, potentially leading to part failure [35]. An upwardly deformed component increases the risk of contact with the coating blade, while a horizontally deformed component may fail to provide a solid base for subsequent deposition [35]. Figure 11 shows a micro-tomographic scan of the 1-mm-thick inclined thin wall, in which the presence of geometric distortion in the last layers is evident. Lastly, examining individual thermograms of the last layers reveals a distortion of the overhang side for the 3 mm sample, albeit to a lesser extent than the 1 mm sample. This explains the absence of significant temperature decrease in the overhang side (Fig. 9b).

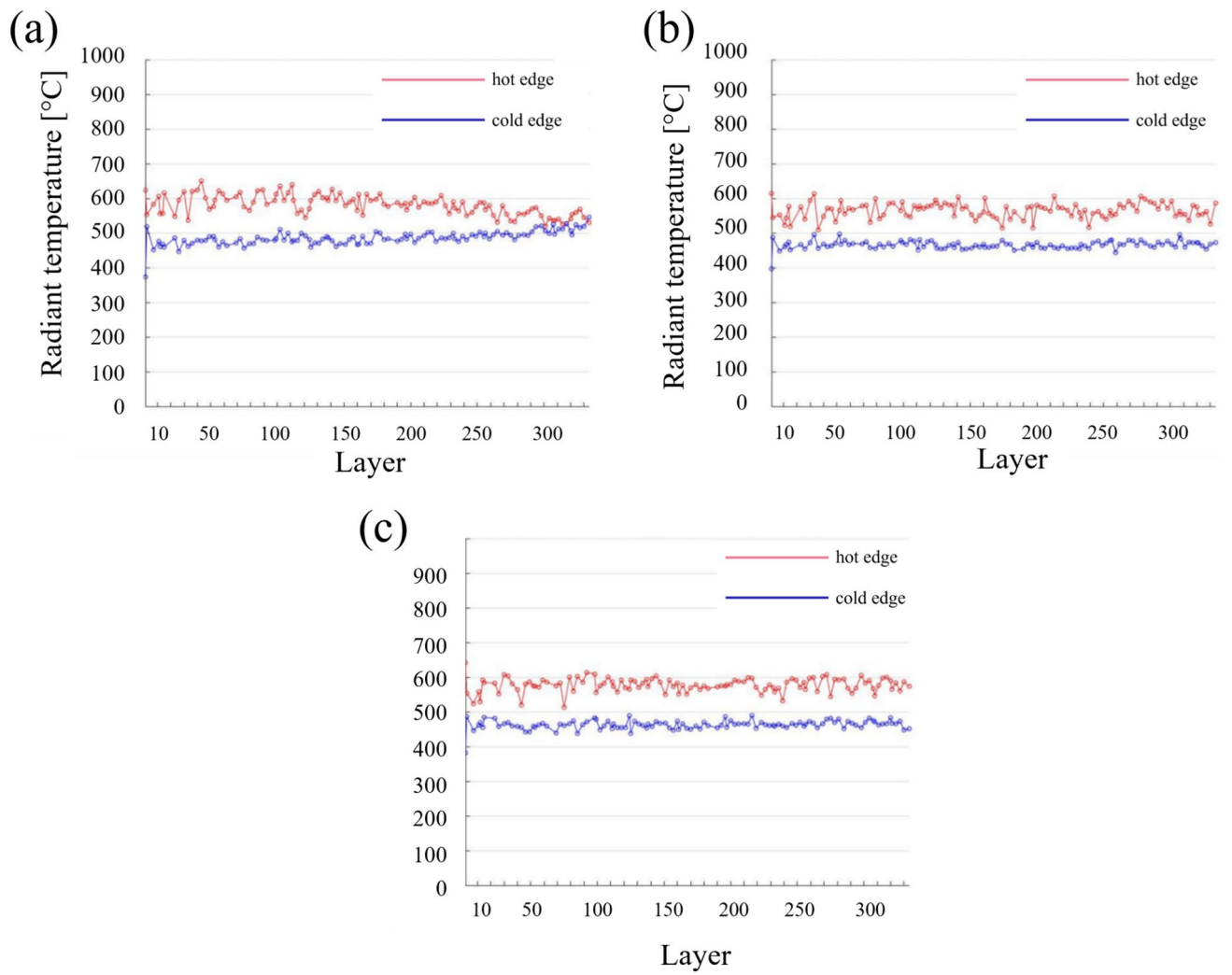


Fig. 9 Average maximum temperature trend of the two major sides of inclined thin walls: **a** 1 mm thickness; **b** 3 mm thickness; **c** 5 mm thickness

3.2.2 Thermal investigation of inclined thin walls during the core scanning phase

The surface temperature distribution between the different samples and varying building heights can be assessed determining the initial and final instants of the core scanning phase. Figure 8c illustrates the maximum temperature distribution reached in each pixel of a generic layer. Similar to straight walls, the presence of overheated zones is evident, which could indicate porosity in the underlying layers, as discussed previously. Voids in the underlying material, containing non-sintered powder, would retain heat, leading to a localized increase in the IR signature on the surface [36]. Overheated areas are marked in the figure by red circles. Analyzing the average maximum temperature reached in all recorded layers of the three walls (Fig. 8d), an initial heating phase due to the 150% increase in powder bed thickness is observed, similarly to samples with orthogonal development from the base platform. As observed with straight walls, the first slice exhibits lower temperatures as only remelting of the exposure slice occurs without additional powder. Subsequently, after the first 10 layers, there is an increasing temperature trend with building height. This behavior is attributed to the phenomenon of 'overheating' characteristic of overhanging structures. The lower thermal conductivity of powdered material compared to bulk metal results in localized 'overheating' and a larger melt pool size [37]. In addition, the powder bed cannot adequately support the liquid metal, leading to unstable melt pool behavior due to gravity, capillarity, turbulent fluid flow, and other related physical phenomena [38]. These factors often result in slag formation and failure on the downward face, negatively impacting surface

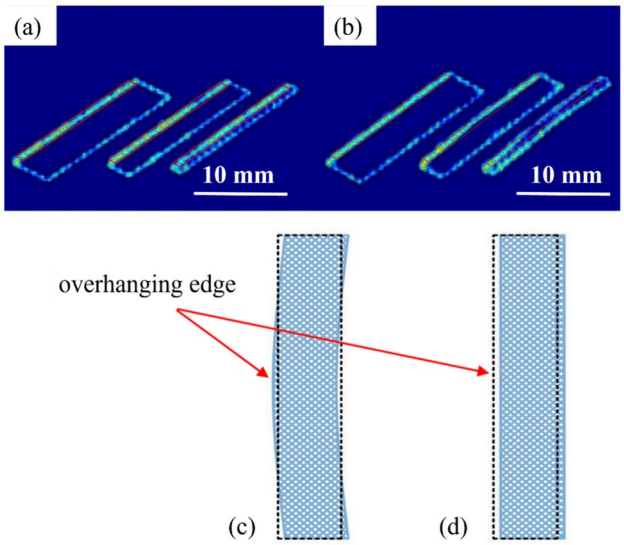


Fig. 10 Representation of the slice geometric configuration before (**a**) and after (**b**) distortion of the 3- and 1-mm-thick walls. The examination area of the protruding side of each sample is shown in red. Diagrammatic depiction of the distortion phenomena in the XY plane, with layer n represented by the blue line and layer n + 1's laser scanning route by the black line. Cases **c** and **d** exhibit distortion and absence of distortion, respectively

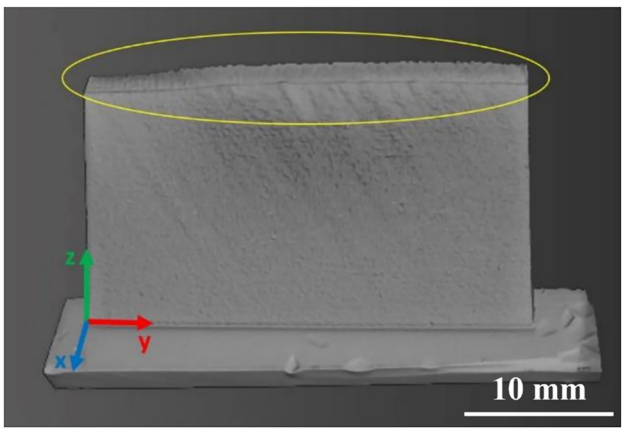


Fig. 11 Micro-tomographic scan of the 1-mm-thick inclined thin wall. The specimen's entire reference system is displayed, with the existence of the last layers' 3D distortions denoted in yellow

roughness and dimensional accuracy [39]. To illustrate this, Fig. 12a, b depicts cross-sections, obtained via micro-tomography, of walls inclined at 45° with thicknesses of 1 mm and 3 mm, respectively (the ideal geometry of the section under examination is outlined in red). These issues are typically addressed through the use of supports, which are load-bearing structures. Supports serve to conduct heat to the base plate, acting as a heat sink or providing mechanical stabilization to the printed part, or both.

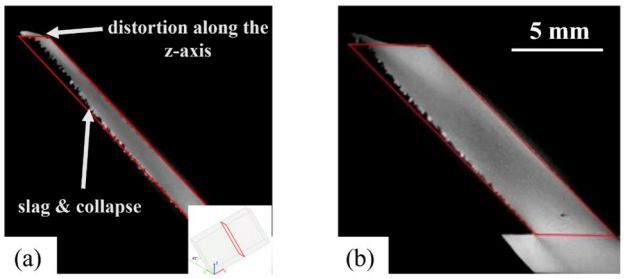


Fig. 12 Micro-tomographic scan of the inclined thin walls: **a** cross-section of the 1 mm thick; **b** cross-section of the 3 mm thick

3.2.3 3D thermograms analysis of inclined thin walls

To understand the surface temperature distribution as the construction height varies, three-dimensional thermograms were generated by overlaying two-dimensional heat maps. This approach provides insights into the vertical development of the fabricated samples and facilitates the detection of overheated zones in three-dimensional space. The theoretical geometry of the individual walls is outlined by black segments. Notably, the last layers of the 1 mm wall exhibit a deviation from the ideal geometry due to the previously discussed distortions. In contrast, the 3-mm and 5-mm-thick samples closely follow the geometry derived from the CAD file (refer to Fig. 13).

4 Conclusions

The study has focused on the thermographic monitoring of the powder bed fusion-laser beam process, aiming to enhance process inspection and quality monitoring in high-tech and precision industries. An optimal setup for in-situ, layer-by-layer thermal monitoring using an off-axis IR thermal camera was implemented, enabling real-time observation of the entire slice during processing. Through the analysis of thermographic data using MATLAB algorithms, several key findings emerged:

- Variations in sample thickness significantly impact maximum temperatures during contouring and core scanning phases.
- The thickness of the powder bed exhibits a discernible effect on process temperatures, in line with the previous literature.
- Geometric distortions, particularly in the overhang zones of inclined walls, result from high thermal stress.
- Three-dimensional thermograms provide comprehensive temperature distributions within parts, facilitating early defect detection and quality control during construction.

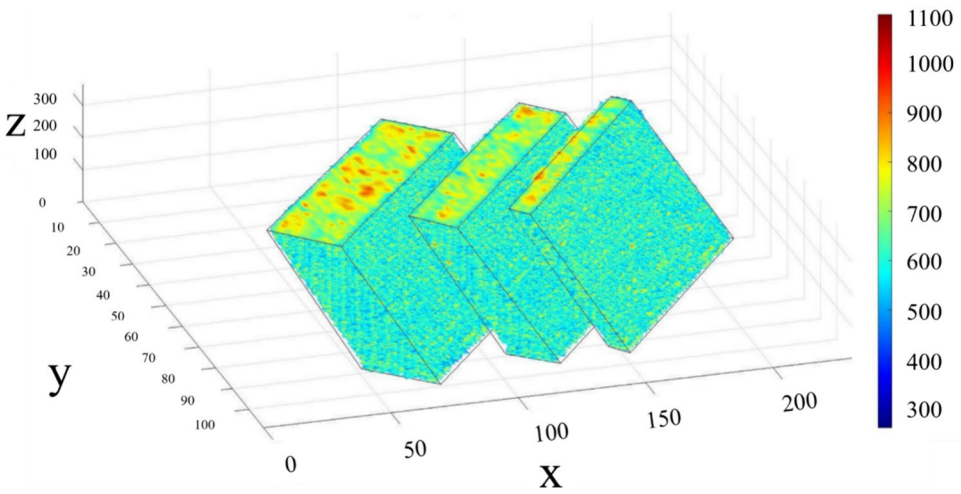


Fig. 13 Inclined thin walls: 3D thermograms

The developed methodology serves a dual purpose:

- It acts as a real-time analysis tool, supporting machine operators in making immediate process stop decisions.
- It facilitates offline post-processing, serving as a diagnostic tool for subsequent qualification steps.

The analysis confirms the effectiveness of this monitoring technique in detecting and localizing defects generated during the process, both in-situ and in-process. Results demonstrate its efficacy in detecting geometric distortions during the construction of overhanging structures.

However, it is imperative to acknowledge the limitations of this work, such as issues related to resolution, speed, and implementation challenges. While these limitations are not unique to this study and are inherent in current monitoring systems, they highlight areas for further research and improvement. Future endeavors could focus on:

- Refining monitoring systems to overcome limitations and improve overall process control and quality monitoring.
- Exploring advanced imaging techniques and sensor technologies to enhance resolution and speed.
- Investigating novel methodologies for real-time process control and quality assurance.

In conclusion, the study offers innovative insights into the challenges and opportunities in additive manufacturing process monitoring. By leveraging advanced monitoring techniques and acknowledging the limitations, the groundwork is laid for further advancements in optimizing the manufacturing process and ensuring product quality.

Acknowledgements The authors would like to thank the late Ing. Fania Palano (co-author), who is no longer with us due to a serious illness, for her significant contribution throughout the experimentation of this work. The authors acknowledge the technical support of Michele Nacucchi, a researcher at ENEA Centro Ricerche Brindisi, for computed tomography analyses. Furthermore, the authors want to thank Ing. Nicola Tarantino for the work carried out during his master's degree thesis, which focused on data analysis for some algorithms discussed and presented in this work. This work was supported by the Italian Ministry of University and Research under the Programme "Department of Excellence" Legge 232/2016 (Grant No. CUP—D93C23000100001).

Author contributions Vito Errico: conceptualization; data curation; formal analysis; investigation; methodology; software; supervision; validation; visualization; writing—original draft; writing—review and editing. Fania Palano: data curation; formal analysis; investigation; methodology; software; supervision. Sabina Luisa Campanelli: conceptualization; data curation; formal analysis; investigation; methodology; supervision; writing—review and editing.

Funding Open access funding provided by Politecnico di Bari within the CRUI-CARE Agreement.

Data availability The authors confirm that the data supporting the findings of this study are available within the article.

Declarations

Conflict of interest The authors declare no conflict of interest.

Open Access This article is licensed under a Creative Commons Attribution 4.0 International License, which permits use, sharing, adaptation, distribution and reproduction in any medium or format, as long as you give appropriate credit to the original author(s) and the source, provide a link to the Creative Commons licence, and indicate if changes were made. The images or other third party material in this article are included in the article's Creative Commons licence, unless indicated otherwise in a credit line to the material. If material is not included in the article's Creative Commons licence and your intended use is not permitted by statutory regulation or exceeds the permitted use, you will need to obtain permission directly from the copyright holder. To view a copy of this licence, visit http://creativecommons.org/licenses/by/4.0/.

References

1. Röttger A, Geenen K, Windmann M et al (2016) Comparison of microstructure and mechanical properties of 316 L austenitic steel processed by selective laser melting with hot-isostatic pressed and cast material. Mater Sci Eng A 678:365–376. https://doi.org/10.1016/J.MSEA.2016.10.012
2. Bourell DL (2016) Perspectives on additive manufacturing. Annu Rev Mater Res 46:1–18. https://doi.org/10.1146/annurev-matsci-070115-031606
3. Rizza G, Galati M, Iuliano L (2024) A multiscale framework for the evaluation of thermal conductivity of sintered powder at the powder bed fusion with electron beam conditions. Prog Addit Manuf. https://doi.org/10.1007/s40964-023-00558-w
4. Grasso M, Colosimo BM (2017) Process defects and in situ monitoring methods in metal powder bed fusion: a review. Meas Sci Technol 28:044005. https://doi.org/10.1088/1361-6501/aa5c4f
5. McCann R, Obeidi MA, Hughes C et al (2021) In-situ sensing, process monitoring and machine control in laser powder bed fusion: a review. Addit Manuf 45:102058. https://doi.org/10.1016/j.addma.2021.102058
6. Hirsch M, Dryburgh P, Catchpole-Smith S et al (2018) Targeted rework strategies for powder bed additive manufacture. Addit Manuf 19:127–133. https://doi.org/10.1016/j.addma.2017.11.011
7. Boschetto A, Bottini L, Vatanparast S (2023) Powder bed monitoring via digital image analysis in additive manufacturing. J Intell Manuf. https://doi.org/10.1007/s10845-023-02091-7
8. Colosimo BM, Grasso M (2020) In-situ monitoring in L-PBF: opportunities and challenges. Procedia CIRP 94:388–391. https://doi.org/10.1016/j.procir.2020.09.151
9. Vu HM, Meiniger S, Ringel B et al (2024) Investigation on surface characteristics of wall structures out of stainless steel 316L manufactured by laser powder bed fusion. Prog Addit Manuf. https://doi.org/10.1007/s40964-023-00559-9
10. Grazia Guerra M, Lafirenza M, Errico V, Angelastro A (2023) In-process dimensional and geometrical characterization of laser-powder bed fusion lattice structures through high-resolution optical tomography. Opt Laser Technol 162:109252. https://doi.org/10.1016/J.OPTLASTEC.2023.109252
11. Scime L, Beuth J (2018) Anomaly detection and classification in a laser powder bed additive manufacturing process using a trained computer vision algorithm. Addit Manuf 19:114–126. https://doi.org/10.1016/j.addma.2017.11.009
12. Baumgartl H, Tomas J, Buettner R, Merkel M (2020) A deep learning-based model for defect detection in laser-powder bed fusion using in-situ thermographic monitoring. Prog Addit Manuf 5:277–285. https://doi.org/10.1007/s40964-019-00108-3
13. Everton SK, Hirsch M, Stravroulakis P et al (2016) Review of in-situ process monitoring and in-situ metrology for metal additive manufacturing. Mater Des 95:431–445. https://doi.org/10.1016/j.matdes.2016.01.099
14. Guerra MG, Errico V, Fusco A et al (2022) High resolution-optical tomography for in-process layerwise monitoring of a laser-powder bed fusion technology. Addit Manuf 55:102850. https://doi.org/10.1016/j.addma.2022.102850
15. Simonds BJ, Tanner J, Artusio-Glimpse A et al (2021) The causal relationship between melt pool geometry and energy absorption measured in real time during laser-based manufacturing. Appl Mater Today 23:101049. https://doi.org/10.1016/J.APMT.2021.101049
16. Ravichander BB, Jagdale SH, Kumar G (2023) Decoupling the effect of orientation on additively manufactured metals by lattice engineering. Prog Addit Manuf. https://doi.org/10.1007/s40964-023-00520-w
17. Gülcan O, Günaydın K, Çelik A, Yasa E (2023) Mechanical properties of laser powder bed fusion produced overhang parts with different support geometries: an experimental study. Prog Addit Manuf. https://doi.org/10.1007/s40964-023-00443-6
18. Yang T, Liu T, Liao W et al (2021) Effect of processing parameters on overhanging surface roughness during laser powder bed fusion of AlSi10Mg. J Manuf Process 61:440–453. https://doi.org/10.1016/j.jmapro.2020.11.030
19. Klingaa CG, Dahmen T, Baier-Stegmaier S et al (2020) Investigation of the roughness variation along the length of LPBF manufactured straight channels. Nondestruct Test Eval 35:304–314. https://doi.org/10.1080/10589759.2020.1785445
20. Paudel BJ, Thompson SM (2019) Localized effect of overhangs on heat transfer during laser powder bed fusion additive manufacturing. In: Solid freeform fabrication 2019: proceedings of the 30th annual international solid freeform fabrication symposium—an additive manufacturing conference, SFF 2019 1175–1189
21. Krauss H, Zeugner T, Zaeh MF (2014) Layerwise monitoring of the selective laser melting process by thermography. Phys Procedia 56:64–71. https://doi.org/10.1016/j.phpro.2014.08.097
22. Krauss H, Zeugner T, Zaeh MF (2015) Thermographic process monitoring in powderbed based additive manufacturing. In: AIP conference proceedings, pp 177–183
23. Bartlett JL, Heim FM, Murty YV, Li X (2018) In situ defect detection in selective laser melting via full-field infrared thermography. Addit Manuf 24:595–605. https://doi.org/10.1016/j.addma.2018.10.045
24. Grünewald J, Reinelt J, Sedlak H, Wudy K (2023) Support-free laser-based powder bed fusion of metals using pulsed exposure strategies. Prog Addit Manuf 8:1631–1640. https://doi.org/10.1007/s40964-023-00429-4
25. Errico V, Fusco A, Campanelli SL (2022) Effect of DED coating and DED + laser scanning on surface performance of L-PBF stainless steel parts. Surf Coat Technol 429:127965. https://doi.org/10.1016/j.surfcoat.2021.127965
26. Errico V, Posa P, Liang L et al (2023) Layer-level AISI 316L–18Ni (300) Maraging multi-material fabrication via laser-powder bed fusion. Mater Sci Eng A 886:145731. https://doi.org/10.1016/j.msea.2023.145731
27. Bartlett JL, Li X (2019) An overview of residual stresses in metal powder bed fusion. Addit Manuf 27:131–149. https://doi.org/10.1016/j.addma.2019.02.020
28. D'AccardiPalumboErrico EDV et al (2023) Analysing the probability of detection of shallow spherical defects by means of pulsed thermography. J Nondestruct Eval 42:27. https://doi.org/10.1007/s10921-023-00936-y
29. Surace R, Errico V, Valori M et al (2023) Laser-powder bed fusion molds without post-processing for micro-injection molding of mini/micro-products. Int J Adv Manuf Technol 127:677–688. https://doi.org/10.1007/s00170-023-11585-w
30. Bayle F, Doubenskaia M (2008) Selective laser melting process monitoring with high speed infrared camera and pyrometer. In: Veiko VP (ed) Proceedings of SPIE, pp 698505-698505–8
31. Liu T, Lough CS, Sehhat H et al (2022) In-situ infrared thermographic inspection for local powder layer thickness measurement in laser powder bed fusion. Addit Manuf 55:102873. https://doi.org/10.1016/J.ADDMA.2022.102873
32. Mohr G, Nowakowski S, Altenburg SJ et al (2020) Experimental determination of the emissivity of powder layers and bulk material in laser powder bed fusion using infrared thermography and thermocouples. Metals (Basel) 10:1546. https://doi.org/10.3390/met10111546
33. Pavlov M, Doubenskaia M, Smurov I (2010) Pyrometric analysis of thermal processes in SLM technology. Phys Procedia 5:523–531. https://doi.org/10.1016/J.PHPRO.2010.08.080

34. Calignano F (2014) Design optimization of supports for overhanging structures in aluminum and titanium alloys by selective laser melting. Mater Des 64:203–213. https://doi.org/10.1016/j.matdes.2014.07.043
35. Wu Z, Narra SP, Rollett A (2020) Exploring the fabrication limits of thin-wall structures in a laser powder bed fusion process. Int J Adv Manuf Technol 110:191–207. https://doi.org/10.1007/s00170-020-05827-4
36. Mostafaei A, Zhao C, He Y et al (2022) Defects and anomalies in powder bed fusion metal additive manufacturing. Curr Opin Solid State Mater Sci 26:100974. https://doi.org/10.1016/J.COSSMS.2021.100974
37. Ranjan R, Ayas C, Langelaar M, van Keulen F (2020) Fast detection of heat accumulation in powder bed fusion using computationally efficient thermal models. Materials 13
38. Wang J, Zhu R, Liu Y, Zhang L (2023) Understanding melt pool characteristics in laser powder bed fusion: an overview of single- and multi-track melt pools for process optimization. Adv Powder Mater 2:100137. https://doi.org/10.1016/J.APMATE.2023.100137
39. Caiazzo F, Alfieri V, Campanelli SL, Errico V (2022) Additive manufacturing and mechanical testing of functionally-graded steel strut-based lattice structures. J Manuf Process 83:717–728. https://doi.org/10.1016/j.jmapro.2022.09.031

Publisher's Note Springer Nature remains neutral with regard to jurisdictional claims in published maps and institutional affiliations.